## Post-Print

This is the accepted version of:

The final publication is available at https://doi.org/10.1364/AO.55.004621

Access to the published version may require subscription.

**When citing this work, cite the original published paper.**

Permanent link to this version
http://hdl.handle.net/11311/999085

# Region-confined restoration method for motion-blurred star image of the star sensor under dynamic conditions

Liheng Ma,[1,2] Franco Bernelli-Zazzera,[2] Guangwen Jiang,[1] Xingshu Wang,[1] Zongsheng Huang,[1] and Shiqiao Qin[1,*]

[1]College of Opto-electronic Science and Engineering, National University of Defense Technology, Changsha 410073, China
[2]Department of Aerospace Science and Technology, Politecnico di Milano, Milan 20156, Italy
*Corresponding author: sqqin8@nudt.edu.cn

**Under dynamic conditions, the centroiding accuracy of the motion-blurred star image decreases and the number of identified stars reduces, which leads to the degradation of the attitude accuracy of the star sensor. To improve the attitude accuracy, a region-confined restoration method, which concentrates on the noise removal and signal to noise ratio (SNR) improvement of the motion-blurred star images, is proposed for the star sensor under dynamic conditions. A multi-seed-region growing technique with the kinematic recursive model for star image motion is given to find the star image regions and to remove the noise. Subsequently, a restoration strategy is employed in the extracted regions, taking the time consumption and SNR improvement into consideration simultaneously. Simulation results indicate that the region-confined restoration method is effective in removing noise and improving the centroiding accuracy. The identification rate and the average number of identified stars in the experiments verify the advantages of the region-confined restoration method.**

## 1. INTRODUCTION

The star sensor is an essential choice for celestial navigation due to its high attitude accuracy [1]. Typically, the attitude with respect to the inertial celestial reference sphere is determined through the following procedures: star image capture, star image preprocessing, star centroid, star identification, and attitude estimation [2]. The attitude accuracy of a star sensor mainly depends on the accuracy of the star centroid. Star image processing before centroiding, thus, is vital for the attitude accuracy of a star sensor. Under static conditions, the star image processing step usually includes the background noise removal, binary operation, and connected component analysis [3]. Compared with the static case, the star image captured under dynamic conditions such as the attitude maneuvers of a satellite, however, is no longer distributed in terms of the Gaussian distribution [4] but is dispersed into a long trail that is severely blurred by the angular motion. In this case, faint stars will be submerged by various additive noises including photon shot noise, readout noise, and dark current noise. Therefore, the number of observed stars will be reduced, and the signal to

noise ratio (SNR) of the star images will drop, which will result in the accuracy decrease of the star centroid and the sensitivity limitation of star magnitude [5]. Consequently, the failure rate of star identification will increase, and the procedure of attitude estimation may not be accomplished.

In order to maintain the centroiding accuracy of a star sensor under dynamic conditions, compensation methods for the motion-blurred star image have been developed. The image motion accommodation method was mentioned by van Bezooijen [6] to maximize the SNR of the blurred images. It was employed to reduce the effect of the motion about the $y$ axis up to 0.42 deg/s in the star sensor AST-301. Ma et al. [7] proposed an extraction method based on the template-correlation matching to identify the blurred star image areas and removes the noise outside the regions simultaneously. The template-correlation matching method was effective in extracting blurred star images; however, its calculation was complicated. Richard et al. [8] described a novel method to compute the predicted star centroids by integrating the star motion during the star integration time period. The calculated

centroids were obtained directly using the center of moment method. Therefore, the final centroids were optimized with the predicted and calculated ones processed by the Kalman filter. However, the star motion integration was realized by the successive projection of the star catalog, and this process was time consuming and complex. Xing *et al.* [9] adopted the extended Kalman filter (EKF) algorithm for the star centroid as well. The EKF equation was established through the calculated centroids and the theoretical ones, which were predicted through the integration of angular velocity of the star sensor during an update period with the initial locations given by the last image frame. In the simulation, the centroiding error for a star with a magnitude of 5 and an angular velocity of 8 deg/s was about 1 pixel. Simultaneously, an extraction window for star centroid was set with the angular velocity measured by the gyro unit. However, no description about the extraction window was given, and the process of star centroid was directly applied in the extraction window. Sun *et al.* [10] adopted the differential method, instead of the gyro unit utilized in [9], to obtain the angular velocity to set the centroiding window. The centroiding accuracy will change according to the window size; therefore, the estimation of the window size was not accurate. The blurred images were not restored, and the improvements for SNR and the accuracy of the star sensor were limited. A denoising method based on the adaptive wavelet threshold for the small angular rate conditions and a modified Wiener restoration method for the large angular rate were proposed by Zhang *et al.* [11]. However, the Wiener filter will result in "ringing" artifacts and noise amplification, which was unfavorable to the star centroid. Moreover, the noise blocks may be identified as stars as well, resulting in an increase of the failure rate of the star identification. In [12], Sun *et al.* studied the Richardson–Lucy (RL) algorithm from the view of the process of Poisson distribution to restore the motion-blurred star image. However, the effect of image noise was not given emphasis, and the process of noise around the blurred image areas was not included or discussed in the simulation and experiments. Based on the RL technique, Ma *et al.* [13] further developed an attitude-correlated frames (ACF) method to improve the attitude accuracy. The ACF method correlated the information of adjacent frames to estimate the attitude, whereas it still highly depended on the process of a single blurred star image.

In this work, based on the existing techniques, a region-confined restoration method for the motion-blurred star image of the star sensor under dynamic conditions is proposed. With the proposed kinematic recursive model, the regions of the blurred star images are determined through the multi-seed-region growing method described in the paper. The process of multi-seed-region growing is accomplished during the exposure period; thus the time consumption of the procedure can be ignored. Then restoration method based on the Bayes theorem is introduced and employed in the region-confined star images with the image degradation model. Simulations and night sky experiments have been carried out, and motion-blurred star images under different dynamic conditions are obtained and processed to validate the approach.

The paper is organized as follows: following this Introduction section, the proposed region-confined restoration method for the motion-blurred star image is presented in Section 2. First, a kinematic recursive model for star image motion is described. Then, the multi-seed-region growing technique is proposed. Finally, the motion-blurred star image restoration approach aided with the degradation model is introduced. Simulations are carried out in Section 3. In Section 4, the experimental results are presented and discussed. Conclusions are drawn in the last section.

## 2. REGION-CONFINED RESTORATION METHOD FOR MOTION-BLURRED STAR IMAGE

### A. Kinematic Recursive Model for Star Image Motion

A kinematic recursive model is derived first to describe the displacement of the star spot with respect to a short sample time $\Delta t$ during the exposure period $T$ and $T = n \cdot \Delta t$ ($n$ is the sample frequency, and it is a positive integer). Supposing that the attitude transform during $\Delta t$ is $\mathbf{C}_{t_0}^{t_0+\Delta t}$, the normalized observed vectors,

$$\mathbf{O}(t_0) = \frac{1}{\sqrt{x(t_0)^2 + y(t_0)^2 + f^2}} \begin{bmatrix} x(t_0) \\ y(t_0) \\ -f \end{bmatrix}, \quad \textbf{(1)}$$

and

$\mathbf{O}(t_0 + \Delta t)$

$$= \frac{1}{\sqrt{x(t_0 + \Delta t)^2 + y(t_0 + \Delta t)^2 + f^2}} \begin{bmatrix} x(t_0 + \Delta t) \\ y(t_0 + \Delta t) \\ -f \end{bmatrix}, \quad \textbf{(2)}$$

at times $t_0$ and $t_0 + \Delta t$, respectively, are therefore correlated by $\mathbf{C}_{t_0}^{t_0+\Delta t}$:

$$\mathbf{O}(t_0 + \Delta t) = \mathbf{C}_{t_0}^{t_0+\Delta t} \cdot \mathbf{O}(t_0), \quad \textbf{(3)}$$

where $f$ is the focus length of the optical lens; $(x(t_0), y(t_0))$ and $(x(t_0 + \Delta t), y(t_0 + \Delta t))$ are the coordinates of the star spot in the star sensor coordinate system at times $t_0$ and $t_0 + \Delta t$, respectively. To obtain the analytic relationship of the observed vectors, Eq. (3) can be derived specifically through the Taylor expansion of $\mathbf{C}_{t_0}^{t_0+\Delta t}$ [14], in which the angular velocity information is included:

$$\mathbf{C}_{t_0}^{t_0+\Delta t} = \mathbf{I}_{3\times3} - (\boldsymbol{\omega}_S \times) \cdot \Delta t$$
$$+ \frac{1}{2}[\boldsymbol{\omega}_S \boldsymbol{\omega}_S^T - \boldsymbol{\omega}_S^T \boldsymbol{\omega}_S \cdot \mathbf{I}_{3\times3} - (\boldsymbol{\omega}_S \times)] \cdot (\Delta t)^2, \quad \textbf{(4)}$$

where $\boldsymbol{\omega}_S = [\omega^x, \omega^y, \omega^z]^T$, $\boldsymbol{\omega}_S^T = [\omega^x, \omega^y, \omega^z]$ and $\boldsymbol{\omega}_S \times$ is the cross product matrix of $\boldsymbol{\omega}_S$. Obviously, the term multiplied by $(\Delta t)^2$ is related to the angular acceleration, the term multiplied by $\Delta t$ corresponds to the angular velocity, and the unit matrix $\mathbf{I}_{3\times3}$ is the initial location of the star spot, respectively. Since the sample time $\Delta t$ during the exposure period is short, the term multiplied by $(\Delta t)^2$ can be neglected. Therefore, the specific form of Eq. (3) is simplified into

$$\mathbf{O}(t_0 + \Delta t) \approx \begin{pmatrix} 1 & \omega^z \Delta t & -\omega^y \Delta t \\ -\omega^z \Delta t & 1 & \omega^x \Delta t \\ \omega^y \Delta t & -\omega^x \Delta t & 1 \end{pmatrix} \cdot \mathbf{O}(t_0). \quad \textbf{(5)}$$

Further, the coordinates of the star spot at time $t_0 + \Delta t$ are

$$\begin{cases} x(t_0 + \Delta t) = \dfrac{x(t_0) + y(t_0)\omega^z \Delta t + f\omega^y \Delta t}{1 - [x(t_0)\omega^y \Delta t - y(t_0)\omega^x \Delta t]/f} \\[2ex] y(t_0 + \Delta t) = \dfrac{y(t_0) - x(t_0)\omega^z \Delta t - f\omega^x \Delta t}{1 - [x(t_0)\omega^y \Delta t - y(t_0)\omega^x \Delta t]/f} \end{cases} \quad \textbf{(6)}$$

Considering that $[x(t_0)\omega^y \Delta t - y(t_0)\omega^x \Delta t]/f \ll 1$ and neglecting the items multiplied by $(\Delta t)^2$, Eq. (6) is simplified into

$$\begin{pmatrix} x(t_0 + \Delta t) \\ y(t_0 + \Delta t) \end{pmatrix} = \begin{pmatrix} 1 & \omega^z \Delta t \\ -\omega^z \Delta t & 1 \end{pmatrix} \begin{pmatrix} x(t_0) \\ y(t_0) \end{pmatrix}$$
$$+ \begin{pmatrix} -\omega^x \Delta t/f & \omega^z \Delta t/f & 0 \\ \omega^y \Delta t/f & 0 & -\omega^x \Delta t/f \end{pmatrix}$$
$$\times \begin{pmatrix} x(t_0)y(t_0) \\ x(t_0)x(t_0) \\ y(t_0)y(t_0) \end{pmatrix} + \begin{pmatrix} f\omega^y \Delta t \\ -f\omega^x \Delta t \end{pmatrix}. \quad \textbf{(7)}$$

Generally, for the $i$th sample time, the new coordinates can be derived from the result of the $(i-1)$th sample time according to Eq. (7):

$$\mathbf{S}_i = \mathbf{P}(\omega_i^z)\mathbf{S}_{i-1} + \mathbf{R}(\omega_i^x, \omega_i^y, \omega_i^z)\mathbf{S}_{i-1}^H + f\Delta t \cdot \mathbf{Q}(\omega_i^x, \omega_i^y), \quad \textbf{(8)}$$

where

$$\mathbf{S}_i = \begin{pmatrix} x(t_0 + i \cdot \Delta t) \\ y(t_0 + i \cdot \Delta t) \end{pmatrix}, \qquad \mathbf{P}(\omega_i^z) = \begin{pmatrix} 1 & \omega_i^z \Delta t \\ -\omega_i^z \Delta t & 1 \end{pmatrix},$$

$$\mathbf{S}_{i-1} = \begin{pmatrix} x(t_0 + (i-1) \cdot \Delta t) \\ y(t_0 + (i-1) \cdot \Delta t) \end{pmatrix}, \qquad \mathbf{Q}(\omega_i^x, \omega_i^y) = \begin{pmatrix} \omega_i^y \\ -\omega_i^x \end{pmatrix},$$

$$\mathbf{R}(\omega_i^x, \omega_i^y) = \begin{pmatrix} -\omega_i^x \Delta t/f & \omega_i^y \Delta t/f & 0 \\ \omega_i^y \Delta t/f & 0 & -\omega_i^x \Delta t/f \end{pmatrix},$$

$$\mathbf{S}_{i-1}^H = \begin{pmatrix} x(t_0 + (i-1) \cdot \Delta t)y(t_0 + (i-1) \cdot \Delta t) \\ x(t_0 + (i-1) \cdot \Delta t)x(t_0 + (i-1) \cdot \Delta t) \\ y(t_0 + (i-1) \cdot \Delta t)y(t_0 + (i-1) \cdot \Delta t) \end{pmatrix}.$$

Therefore, a kinematic recursive model of star image motion is obtained, and the coordinates of star images at different sample times can be calculated through this model. The angular velocities can be obtained through strap-down gyroscopes or other estimation methods [15–17].

## B. Multi-Seed-Region Growing

In order to determine the pixels of the motion-blurred star image, a multi-seed-region growing method is proposed. The star image spot in the image sensor is generally defocused in $3 \times 3$ pixels or $5 \times 5$ pixels to get a high centroiding accuracy, and a group of $3 \times 3$ pixels is adopted in our work. For each star image in the image sensor, the central pixel $\mathbf{S}_0$ in the $3 \times 3$ pixel group $G_0(x, y)$ is regarded as the seed pixel at the beginning of the exposure time. The pixels containing the motion-blurred star image are found through the growing of the seed pixels that are updated with the kinematic recursive model presented in subsection 2.A. A virtual logic image frame $V(x, y)$ of the same size as the real captured star image frame $R(x, y)$ is generated previously. The process of multi-seed-region growing is

performed in the virtual image frame during the exposure time; therefore, no extra consumption of time is needed. The detailed process of the multi-seed-region growing method is given as follows:

Step 1: Generate a virtual logic image frame $V(x, y)$ whose size is the same as the real one and all the values are set to zero.
Step 2: With a prediction of the initial attitude [9], the seed pixels of all the star image spots are obtained through the projection of the referenced star catalog (Sky 2000 for example):

$$\text{Seeds} = \{\mathbf{S}_0^1, ..., \mathbf{S}_0^j, ..., \mathbf{S}_0^k\} \qquad (1 \le j \le k), \quad \textbf{(9)}$$

where the superscripts $j$ and $k$ are positive integers, and they denote the number of star image spots in an image frame.
Step 3: The eight neighbor pixels of the seed pixel $\mathbf{S}_0^j$ and itself form the $3 \times 3$ pixel group $G_0^j(x, y)$. Therefore a set of pixel groups is obtained:

$$\text{Groups} = \{\mathbf{G}_0^1, ..., \mathbf{G}_0^j, ..., \mathbf{G}_0^k\} \qquad (1 \le j \le k). \quad \textbf{(10)}$$

Step 4: Update the seed pixels with the kinematic recursive model presented in subsection 2.A and then form a new pixel group with the eight neighbor pixels generated from the seed pixel. Thus, Eqs. (9) and (10) are updated to

$$\text{Seeds} = \{\mathbf{S}_1^1, ..., \mathbf{S}_1^j, ..., \mathbf{S}_1^k\} \qquad (1 \le j \le k), \quad \textbf{(11)}$$

and

$$\text{Groups} = \{\mathbf{G}_1^1, ..., \mathbf{G}_1^j, ..., \mathbf{G}_1^k\} \qquad (1 \le j \le k). \quad \textbf{(12)}$$

Step 5: Merge the pixel groups generated from the same star and update the current group set with the merging results. Take the $j$th star, for example:

$$G_1^j(x, y) = G_0^j(x, y) \cup G_1^j(x, y). \quad \textbf{(13)}$$

Step 6: Repeat steps 4 and 5 until the end of the exposure time. Therefore, the pixel region of the $j$th star image is

$$G_n^j(x, y) = G_{n-1}^j(x, y) \cup G_n^j(x, y). \quad \textbf{(14)}$$

Step 7: Set the values of all the pixels in the extracted pixel regions to 1.
Step 8: Remove the background noises of the real captured star image frame $R(x, y)$ by a threshold method [18].
Step 9: Obtain the blurred star image regions $B(x, y)$ by the multiplication between the virtual image frame and the real captured one:

$$B(x, y) = R(x, y) \cdot V(x, y). \quad \textbf{(15)}$$

A schematic diagram about the multi-seed-region growing method is given in Fig. 1. Obviously, the sample frequency should be appropriately selected to ensure that all the blurred pixels are included in the region and to reduce the processing time at the same time. Since the focus length is much bigger than the radius of the motion around the $z$ axis, an experimental estimation formula for the sample frequency, without the angular velocity around the $z$ axis, is given:

$$n = \left\lfloor \frac{\sqrt{\omega_x^2 + \omega_y^2} \cdot T}{\text{FOV}} \cdot N \right\rfloor, \quad \textbf{(16)}$$

where the bracket symbol "$\lfloor \ \rfloor$" denotes the operation of rounding down to the nearest integer, FOV is the field of view, and $N$ is the number of pixels across the focal plane.
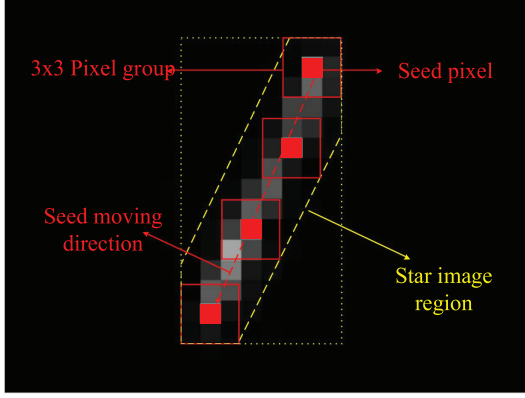
**Fig. 1.** Schematic diagram of the multi-seed-regions growing method.

Through the above steps, the regions of the motion-blurred star images are obtained. The values of pixels beyond the regions are set to zero; therefore, noises outside the regions are removed completely. Thus, the process of motion-blurred star image restoration can be implemented further with a higher centroiding accuracy.

## C. Motion-Blurred Star Image Restoration

Different from the common image restoration which emphasizes the visual effect recovery, however, restoration of the motion-blurred star image concentrates on the pixel-level image reconstruction that is much more refined. Here, we referenced to the RL algorithm [19,20] from the view of the Bayes theorem and employed the algorithm to restore the motion-blurred star images. As the point spread function (PSF) is required in the restoration, the degradation model for the motion-blurred star image is introduced first to obtain the PSF, and then the restoration process is implemented.

### 1. Image Degradation Model

The motion-blurred image $g(x, y)$ under dynamic conditions is expressed as

$$g(x, y) = \int_0^T f(x-x(t_0 + t), y-y(t_0 + t))\mathrm{d}t, \tag{17}$$

where $x(t_0 + t)$ and $y(t_0 + t)$ are the seed pixel of the star image as described in subsection 2.B. Applying the Fourier transform to Eq. (17),

$$G(u, v) = \int_{-\infty}^{\infty} g(x, y)e^{-j2\pi(ux+vy)}\mathrm{d}x\mathrm{d}y$$
$$= F(u, v) \int_0^T e^{-j2\pi[ux(t_0+t)+vy(t_0+t)]}\mathrm{d}t. \tag{18}$$

The Fourier transform of the PSF can be written as

$$H(u, v) = \int_0^T e^{-j2\pi[ux(t_0+t)+vy(t_0+t)]}\mathrm{d}t. \tag{19}$$

Thus, the degradation model of the motion-blurred image can be described in the Fourier term with the additive noise item $N(u, v)$:

$$G(u, v) = F(u, v)H(u, v) + N(u, v). \tag{20}$$

According to the convolution theory, Eq. (20) can be rewritten in the spatial domain:

$$g(x, y) = f(x, y) \otimes h(x, y) + n(x, y), \tag{21}$$

where the symbol "$\otimes$" is the convolution operation. Thus, the image degradation model is obtained.

### 2. Bayes Theorem Based Image Restoration Strategy

The numerical values of a point of the original image $f(x, y)$, the blurred image $g(x, y)$, and the PSF $h(x, y)$ are considered as the frequency of occurrence of an event at that point [19]. Therefore, the Bayes theorem can be used to obtain the original image when the blurred image and the PSF are given. Take one dimension of the image for simplification. After the removal of the additive noise, the degradation model can be rewritten as

$$g(x) = f(x) \otimes h(x). \tag{22}$$

Considering the conditional probability $p(f_i|g_k)$ when the blurred image spot $g_k$ is given,

$$p(f_i|g_k) = \frac{p(g_k|f_i)\pi(f_i)}{\sum_j p(g_k|f_j)\pi(f_j)}, \tag{23}$$

where $f_i$, $f_j$, and $g_k$ are the numerical values of the $i$th, $j$th, and $k$th pixels of images $f$, $f$, and $g$, respectively. According to the dependence of $g_k$ and the full probability formula, Eq. (24) is obtained:

$$p(f_i) = \sum_k p(f_i \cdot g_k) = \sum_k p(f_i|g_k)p(g_k). \tag{24}$$

Substituting Eq. (23) into Eq. (24), we can obtain that

$$p(f_i) = \sum_k \frac{p(g_k|f_i)p(f_i)p(g_k)}{\sum_j p(g_k|f_j)p(f_j)}, \tag{25}$$

where $p(f_i)$ in the right side is also the solution; therefore, we can rewrite Eq. (25) into the iteration form and give a guess at the initial solution:

$$p_{r+1}(f_i) = p_r(f_i)\sum_k \frac{p(g_k|f_i)p(g_k)}{\sum_j p(g_k|f_j)p_r(f_j)}. \tag{26}$$

Substituting $p(g_k|f_i) = p(h_{i,k})$, $p(f_i) = f_i/f$, $p(h_{j,k}) = h_{j,k}/h$, and $p(g_k) = g_k/g = g_k/f$ into Eq. (26), it can be simplified into

$$f_{i,r+1} = f_{i,r}\sum_k \frac{h_{i,k} \cdot g_k}{\sum_j h_{j,k} \cdot f_{j,r}}. \tag{27}$$

The convergence of the iteration has to be estimated in order to stop the restoration. The process of star centroid is executed after a restoration iteration, and the centroiding results of two successive star image frames are compared with the adaptive thresholds $\varepsilon_x(\omega_y)$ and $\varepsilon_y(\omega_x)$:

$$\begin{cases} |x_{r+1} - x_r| \le \varepsilon_x(\omega_y) \\ |y_{r+1} - y_r| \le \varepsilon_y(\omega_x) \end{cases}. \tag{28}$$

The difficulty of restoration is proportional to the angular velocity; therefore, a good strategy to stop the restoration iteration is to set a threshold that is a function of angular velocities. The type of function depends on the requirements of the centroiding accuracy and the update frequency of the star

sensor. If a high update frequency is required, then the time consumption in the restoration should be reduced; thus, the times of iteration should be reduced, resulting in a big threshold. Here, a step function is a good choice. For example, $\varepsilon_x = \Delta\varepsilon$ when $\omega_y \leq 1$ deg/s, $\varepsilon_x = 2 \cdot \Delta\varepsilon$ when $1 < \omega_y \leq 2$ deg/s, and $\Delta\varepsilon$ is fixed to 0.05 pixel perhaps.

The star image regions only occupy a small fraction of the whole image frame, and the iteration algorithm is implemented in the extracted star image regions obtained in subsection 2.B. Through this restoration strategy, the motion-blurred star image will be restored more efficiently, which is helpful in maintaining the update frequency of the star sensor. With high SNR in the restored star images, the centroiding accuracy will be improved.
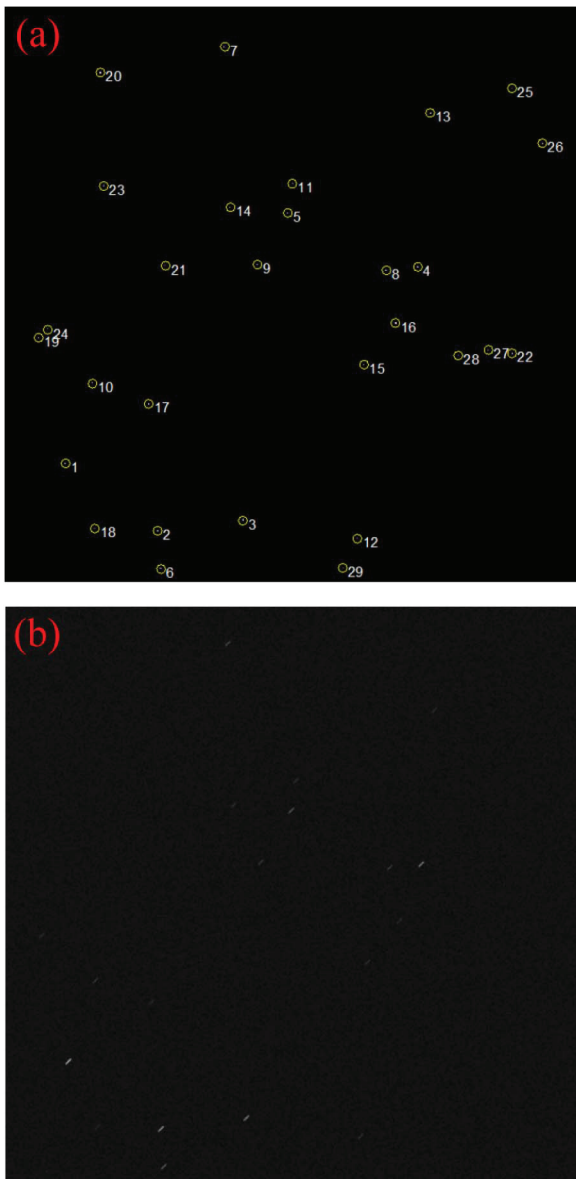
**(a)**

**(b)**

**Fig. 2.** Simulated star image under (a) static condition and (b) dynamic condition. The grayscale is properly chosen in order to better show the star image.

## 3. SIMULATION

Simulations under different dynamic conditions and noise levels are implemented to verify the proposed region-confined restoration method. We suppose that the angular velocity around the $z$ axis is 0 and that the velocities around the $x$ and $y$ axes are constant and equal. Their resultant velocity is sequentially set to 0.5 deg/s, 1 deg/s, and 1.5 deg/s in order to simulate different dynamic conditions. With the given attitude information, the stars in the inertial catalog under the sensitive magnitude threshold, which is calculated through the SNR limitation of the extraction of the blurred star image [4], are projected into the image focus plane of the star sensor with a FOV of 14 deg ×14 deg, a focus length of 25.6 mm, and an exposure time of 180 ms. With the coordinates of the projected star images, the motion degradation model is adopted to generate the motion-blurred star image [5,21], to which Gaussian white noise is subsequently added. The standard deviation of the noise gray level is sequentially set to 20, 40, 60, 80, and 100 (the saturated gray level of a pixel is 65535). In this way, motion-blurred star images are simulated. The region-confined restoration method is employed, first to extract the blurred star image areas and remove the noise around them, and then improve the SNR of the star image by the restoration. Using the center of moment method, star centroids are obtained for comparison from the restored image by the

**Table 1.  Star Information of the Star Image Frame**

| Star No. | Right Ascension/° | Declination/° | Mag./ Mv | Locations | |
| --- | --- | --- | --- | --- | --- |
| | | | | x/pixel | y/pixel |
| 1 | 266.6146 | 27.7206 | 3.42 | 109.48 | 814.16 |
| 2 | 269.4411 | 29.2478 | 3.70 | 273.95 | 934.09 |
| 3 | 271.8856 | 28.7624 | 3.84 | 425.76 | 914.78 |
| 4 | 275.9245 | 21.7697 | 3.85 | 736.88 | 463.58 |
| 5 | 272.1895 | 20.8145 | 4.37 | 505.53 | 368.13 |
| 6 | 269.6256 | 30.1892 | 4.41 | 278.94 | 1001.01 |
| 7 | 270.0142 | 16.7509 | 4.67 | 392.58 | 71.40 |
| 8 | 275.0746 | 21.9612 | 4.93 | 680.82 | 469.49 |
| 9 | 271.5079 | 22.2188 | 4.99 | 451.26 | 460.11 |
| 10 | 267.2047 | 25.6228 | 5.10 | 157.34 | 670.60 |
| 11 | 272.2202 | 20.0452 | 5.11 | 513.45 | 315.30 |
| 12 | 275.2542 | 28.8699 | 5.13 | 628.98 | 947.36 |
| 13 | 275.7043 | 17.8266 | 5.25 | 759.78 | 189.76 |
| 14 | 270.5960 | 20.8336 | 5.26 | 402.70 | 358.46 |
| 15 | 274.7945 | 24.4460 | 5.28 | 640.78 | 638.01 |
| 16 | 275.5362 | 23.2851 | 5.42 | 698.01 | 564.39 |
| 17 | 268.8549 | 26.0499 | 5.47 | 258.11 | 708.45 |
| 18 | 267.5953 | 29.3221 | 5.52 | 161.16 | 930.38 |
| 19 | 265.6181 | 24.5640 | 5.56 | 62.30 | 590.11 |
| 20 | 266.7835 | 17.6970 | 5.62 | 172.00 | 117.65 |
| 21 | 268.9617 | 22.4642 | 5.62 | 286.99 | 460.99 |
| 22 | 278.8766 | 23.6055 | 5.64 | 906.05 | 617.50 |
| 23 | 267.1032 | 20.5654 | 5.70 | 177.92 | 319.25 |
| 24 | 265.8398 | 24.3278 | 5.73 | 77.53 | 574.58 |
| 25 | 277.7685 | 16.9285 | 5.76 | 905.18 | 146.07 |
| 26 | 278.8025 | 18.2034 | 5.79 | 960.03 | 244.45 |
| 27 | 278.1923 | 23.6168 | 5.86 | 862.62 | 611.48 |
| 28 | 277.3987 | 23.8662 | 5.88 | 809.93 | 621.03 |
| 29 | 274.9669 | 29.6663 | 6.00 | 604.33 | 1000.42 |

region-confined restoration method and the common used RL restoration method. For the star image corresponding to each angular velocity and noise gray level, 100 random simulations are carried out, and their average value is regarded as the final result. Figure 2 shows the simulated star image under static conditions and dynamic conditions. Table 1 gives the star information of the star image frame in detail.

In Fig. 3, with the proposed region-confined restoration method, simulation results of a blurred star image cropped from the simulated star image frame are shown in detail. The angular velocity is set to 1 deg /s, and the noise level is set to 60. Figure 3(a) is the blurred star image with additive noises, and Figs. 3(b) and 3(c) are shown in color scale and three-dimensional (3D) bar plot. Through the seed growing method, the seed pixels are found and marked with red circles in Fig. 3(d). Therefore, the blurred star image region can be obtained, and the noise around it can be removed as shown in Figs. 3(e) and 3(f). The restored images are shown in Figs. 3(g)–3(i). It can be seen that the energy of the star image

is concentrated. The highest gray value in the blurred star image is about 3500 after the region-confined restoration; however, it reaches up to 23,000 in the restored image. Therefore, the SNR of the star image area is markedly improved.

The blurred star images are processed by the proposed region-confined restoration method and the common used RL method. Centroiding results of the blurred star image under different angular velocities and noise gray levels are shown in Fig. 4. The stars in Fig. 4 are sorted by magnitude in ascending order and indexed by positive numbers accordingly with the star number in Table 1. In Figs. 4(a), 4(c), and 4(e), centroiding results are obtained from the restored image by the common used RL method, and the angular velocities are set to 0.5, 1, and 1.5 deg /s, respectively. For each angular velocity, the noise gray level changes from 20 to 100 with a step of 20. When the noise gray level increases and the angular velocity reaches up to 1.5 deg /s, the centroiding error is over 1 pixel; thus, the centroiding result is considered to be a failure. Figures 4(b), 4(d), and 4(f) are centroiding results processed
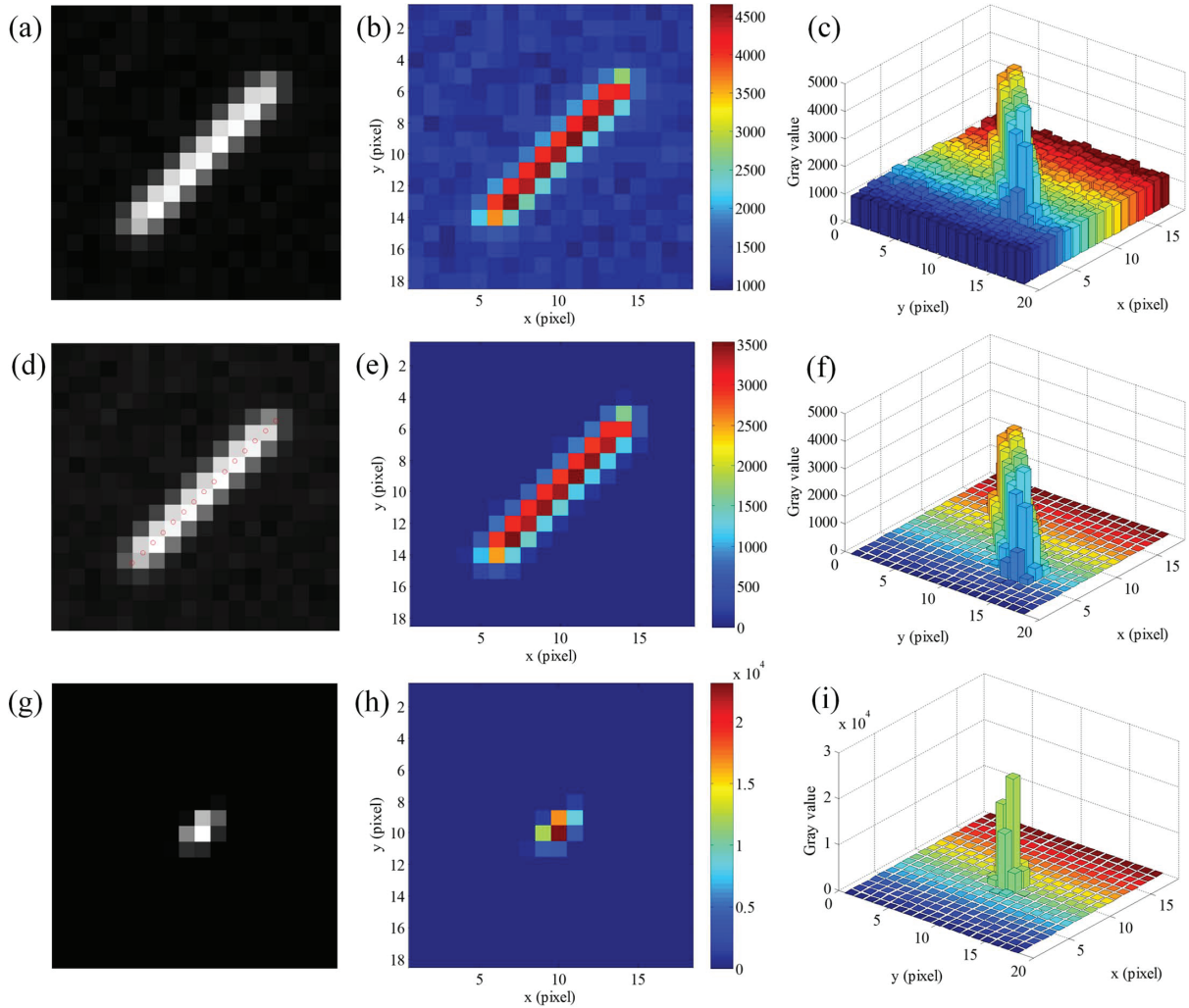


**Fig. 3.** Simulation results of a blurred star image processed by the region-confined restoration method. (a) Blurred star image with additive noise; the angular velocity is set to 1°/s and the noise level is set to 60. (d) Blurred star image after seed growing. (g) Image restoration result from the extracted blurred star image area. (b) and (c) are the detailed views of (a) in color scale and 3D bar plots. (e) and (f) are the detailed views of (d) in color scale and 3D bar plots; the noise around the extracted regions is removed.

with the proposed region-confined restoration method, and the angular velocities are set to 0.5, 1, and 1.5 deg /s, respectively. It can be seen from the comparisons of Figs. 4(a) and 4(b), Figs. 4(c) and 4(d), and Figs. 4(e) and 4(f) that, with the region-confined restoration method, the centroiding error is much smaller than that of the commonly used RL method. When the angular velocity and noise gray value increase, the advantage is more obvious. Take the curve "noise gray level = 20" in Figs. 4(a)–4(d) for example, the centroiding errors in Figs. 4(a) and 4(b) are almost the same; however, the difference is remarkable in Figs. 4(c) and 4(d) since the angular velocity increases from 0.5 to 1 deg /s. With the region-confined restoration method, the star centroid can be implemented in high angular velocities and noise levels as shown in Fig. 4(f). As the angular velocity increases from 0.5 to 1.5 deg /s, the SNR of the motion-blurred stars decreases; as a result, the number of extracted stars reduces as can be seen from the number reduction from Figs. 4(a)–4(f).
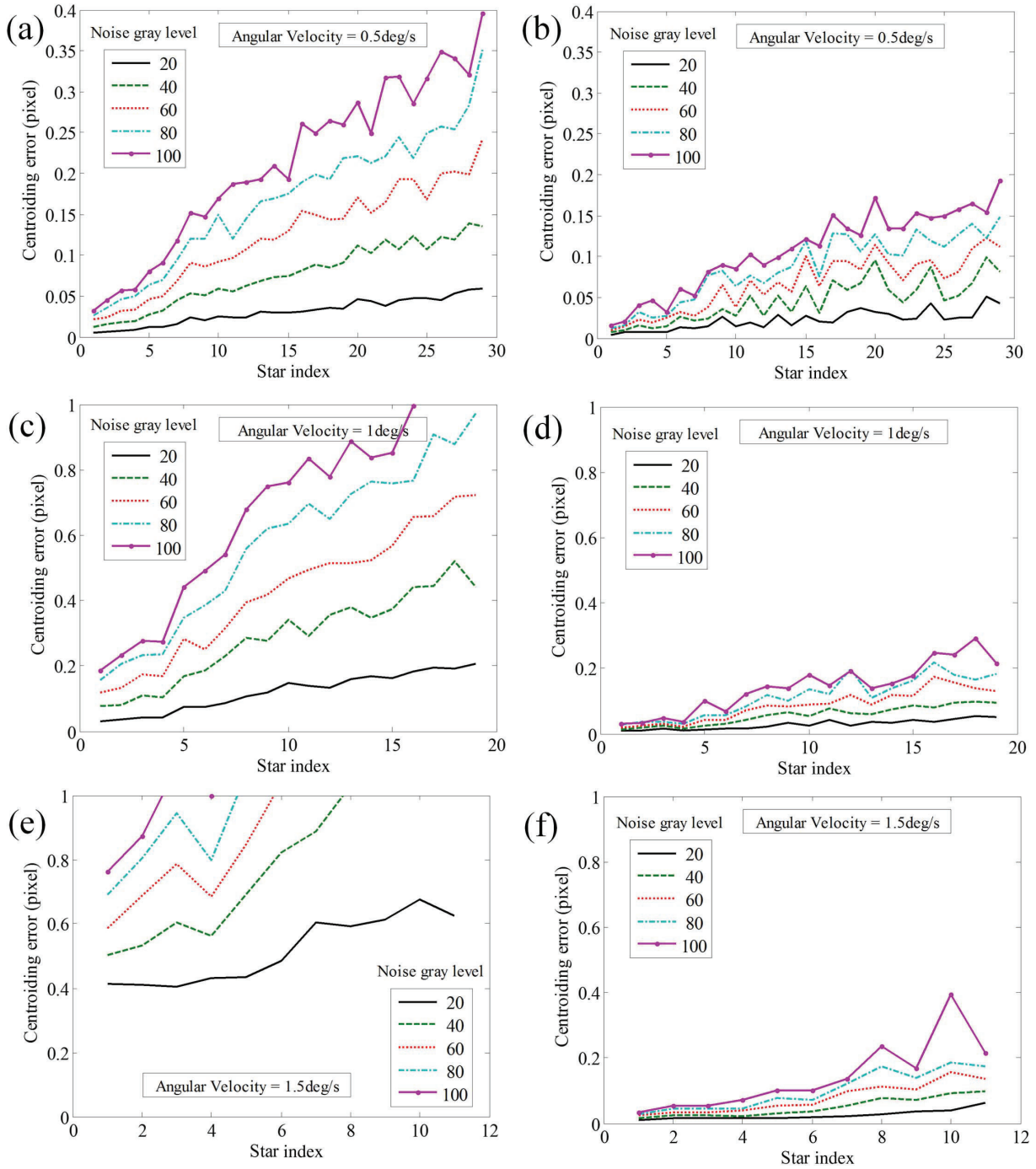


**Fig. 4.** Centroiding results of the blurred star images under different angular velocities and noise levels (stars are numbered and sorted by magnitude in ascending order). (a), (c), and (e) are centroiding results processed with the commonly used RL method. (b), (d), and (f) are centroiding results processed with the proposed region-confined restoration method.

It can be seen in each subfigure of Fig. 4 that the centroiding error increases following the star magnitude (stars are numbered and sorted by magnitude in ascending order), that is, the SNR of the motion-blurred star images.

## 4. EXPERIMENTAL RESULTS AND DISCUSSION

In order to verify the validation of the proposed method, night sky experiments under different dynamic conditions were implemented at the summit of the Heimifeng National Forest Park (N28.2218°, E112.9924°; altitude: 590.50 m), where there is no stray light from the city. The star images were captured by a ground-used star sensor with a FOV of 14 deg ×14 deg, a focus length of 25.6 mm, and an exposure time of 180 ms. The parameters are the same as the ones in the simulation, and the experimental setup is the same one in our previous paper [13] as shown in Fig. 5. The gyro unit with three laser gyroscopes orthogonally assembled and the star sensor are mounted on a 2D turntable with its $x$ axis locked. The $x$–$y$ plane of the turntable is tilted to the horizontal plane as shown. Motion-blurred star images are generated through the rotation of the 2D turntable around its $z$ axis. Synchronization between the gyro unit and the star sensor is supplied by a Global Positioning System unit made by NovAtel (product model: OEM615). The gyro unit is utilized to provide the initial attitude for the projection of the star catalog and the angular velocity for the motion-blurred star image restoration.

To better indicate the advantages of the region-confined restoration method, star image frames were captured under variable angular velocities, and the angular velocities measured by the gyro unit were transformed to the star-sensor-based coordinates through the mounting matrix $\mathbf{C}_g^s$ [15], which was calibrated previously. Figure 6(a) shows the angular velocity of the star sensor in the experiment. The maximum angular
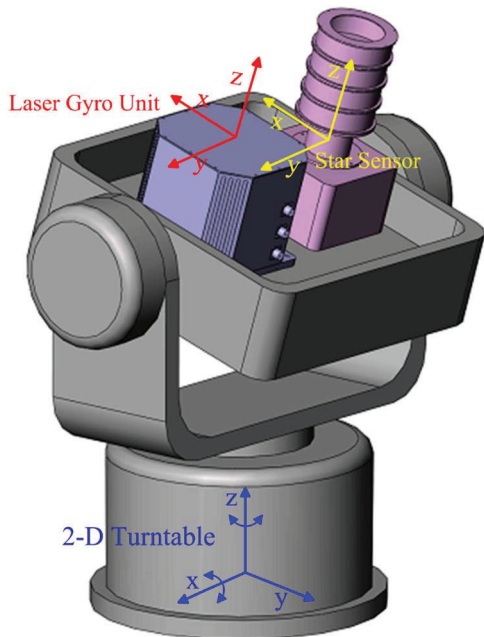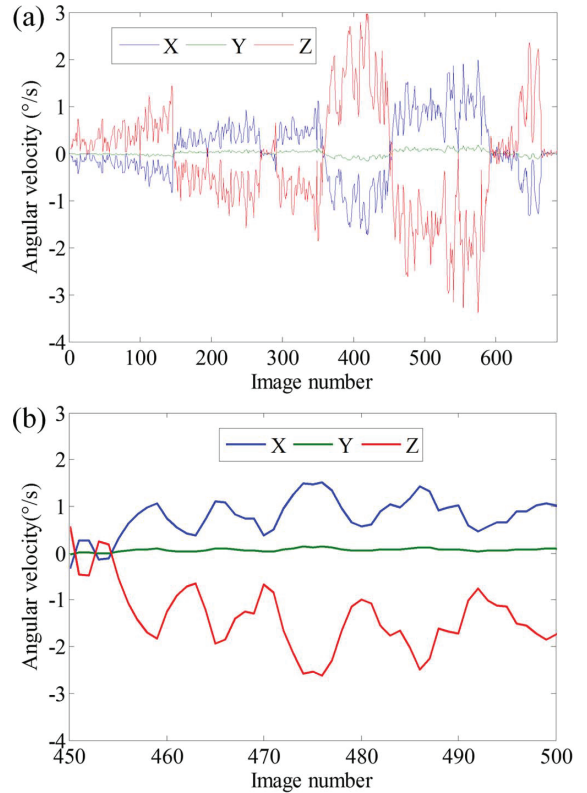


**Fig. 6.** Angular velocity of the star sensor. (b) is a magnification of (a) in order to display fine details.

velocities about the $x$, $y$, and $z$ axes are 1.8, 0.17, and 3.3 deg /s, respectively.

In the experiment, the identification rate and the average number of the identified stars are utilized to evaluate the performances of our proposed method. The center of moment method is used for the star centroid, and the grid algorithm [22] is employed for the star identification. A frame is called the identified frame here once there are stars in a frame that are identified, since this frame will contribute to the identification rate. The motion-blurred star images are processed with the proposed region-confined restoration approach and the commonly used RL method, respectively. The identification rate and the average number of the identified stars are listed in Table 2, and the results without our method are also given for comparison.

With our method, the identification rate is up to 98.24%, and the average number of the identified stars is up to 15.21, whereas the rate drops to 29.17% and the number decreases to 10.75 without our method. Here, merely the identified frames are counted in the calculation of the average number of the identified stars, as listed in the third and sixth columns of Table 2. When we count all the captured frames, the average number of the identified stars will be less than 4 without our method; however, the number can be up to 14.94 with our method, as listed in the fourth and seventh columns of Table 2. Taking a further look at the identified frames without our method, we can find that the frames were captured at an angular velocity that is much lower (<0.3°/s both around the $x$ and $y$ axes). From this comparison, we can see that our method



**Fig. 5.** Experimental setup.

**Table 2. Star Identification Result of the Experiment**

| | With Our Method | | | Without Our Method | |
|---|---|---|---|---|---|
| Identification rate | Average Number of Identified Star[a] | Average Number of Identified Star[b] | Identification Rate | Average Number of Identified Star[a] | Average Number of Identified Star[b] |
| 98.24% | 15.21 | 14.94 | 29.17% | 10.75 | 3.13 |

[a]Only the identified frames are counted in.
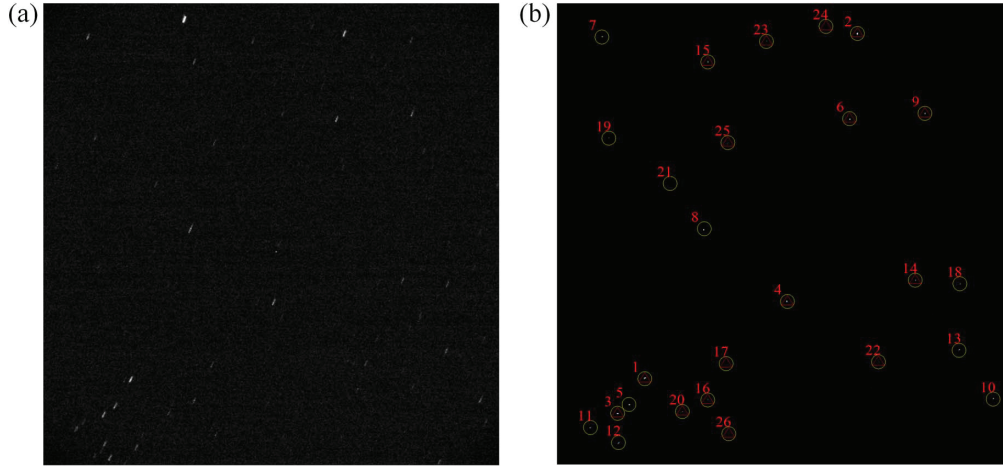[b]All the captured frames are counted in.



**Fig. 7.** (a) Original motion-blurred star image; the grayscale is properly chosen in order to better show the star image. (b) Processed image and identification result with our method. Extracted stars are marked in circles and numbered; identified stars are marked in triangles.

is more effective in the processing of the motion-blurred star image, and it is adaptive to different dynamic conditions.

Figure 7(a) is a star image frame captured in the experiment. The angular velocity of this frame is 1.05°/s around the $x$ axis, 0.48°/s around the $y$ axis, and 0.62°/s around the $z$ axis on average. The center of the star image moves about 16 pixels during the exposure time, which leads to the star image being severely motion-blurred. The energy of the star is dispersed into tens of pixels, resulting in an SNR decrease of the star image. It has been a knotty problem to extract the elongated star spots, let alone to identify them. Figure 7(b) is the blurred image processed by our method. Twenty-six blurred star image regions are reserved, which are marked in circles and numbered in the figure. Among the extracted star images, 16 stars marked in triangles have been identified, and the identification results of this frame are listed in Table 3. For comparison, the

**Table 3. Star Identification Result of a Star Image Frame**

| | | | | | With Our Method | | Without Our Method | |
|---|---|---|---|---|---|---|---|---|
| Star No. | Right Ascension/° | Declination/° | Mag./Mv | Star No. in catalog | $x$/pixel | $y$/pixel | $x$/pixel | $y$/pixel |
| 1 | 186.7345 | 28.2684 | 4.34 | 151531 | 201.7331 | 846.4074 | 202.1422 | 845.4039 |
| 2 | 188.4356 | 41.3575 | 4.25 | 152639 | 687.1710 | 70.1666 | 688.1929 | 69.5211 |
| 3 | 186.7471 | 26.8257 | 4.96 | 151540 | 139.7293 | 925.9344 | 141.9623 | 927.8414 |
| 4 | 184.1256 | 33.0615 | 4.99 | 149764 | 526.7357 | 673.0036 | 527.8864 | 673.1456 |
| 6 | 186.4622 | 39.0186 | 5.02 | 151360 | 669.6446 | 262.4497 | Fail | Fail |
| 9 | 184.0315 | 40.6602 | 5.67 | 149694 | 841.8554 | 249.0120 | Fail | Fail |
| 14 | 180.4145 | 36.0421 | 5.59 | 147305 | 819.8458 | 625.1476 | 822.9934 | 623.4628 |
| 15 | 192.5448 | 37.5169 | 5.88 | 155410 | 345.9941 | 133.3456 | 348.2347 | 135.7823 |
| 16 | 184.3774 | 28.9372 | 5.71 | 149906 | 345.3538 | 895.0842 | Fail | Fail |
| 17 | 184.6318 | 30.2490 | 6.23 | 150091 | 386.4230 | 813.4834 | Fail | Fail |
| 20 | 184.8730 | 28.1569 | 6.38 | 150258 | 288.0894 | 921.8006 | Fail | Fail |
| 22 | 179.8231 | 33.1670 | 5.95 | 146892 | 736.1654 | 810.7894 | Fail | Fail |
| 23 | 191.2475 | 39.2789 | 5.96 | 154522 | 479.9254 | 85.8674 | Fail | Fail |
| 24 | 189.6928 | 40.8747 | 6.35 | 153418 | 615.0000 | 53.9815 | Fail | Fail |
| 25 | 189.8203 | 35.9520 | 6.40 | 153521 | 391.4312 | 315.2433 | Fail | Fail |
| 26 | 183.0042 | 28.5363 | 6.46 | 149041 | 394.3138 | 971.6032 | Fail | Fail |
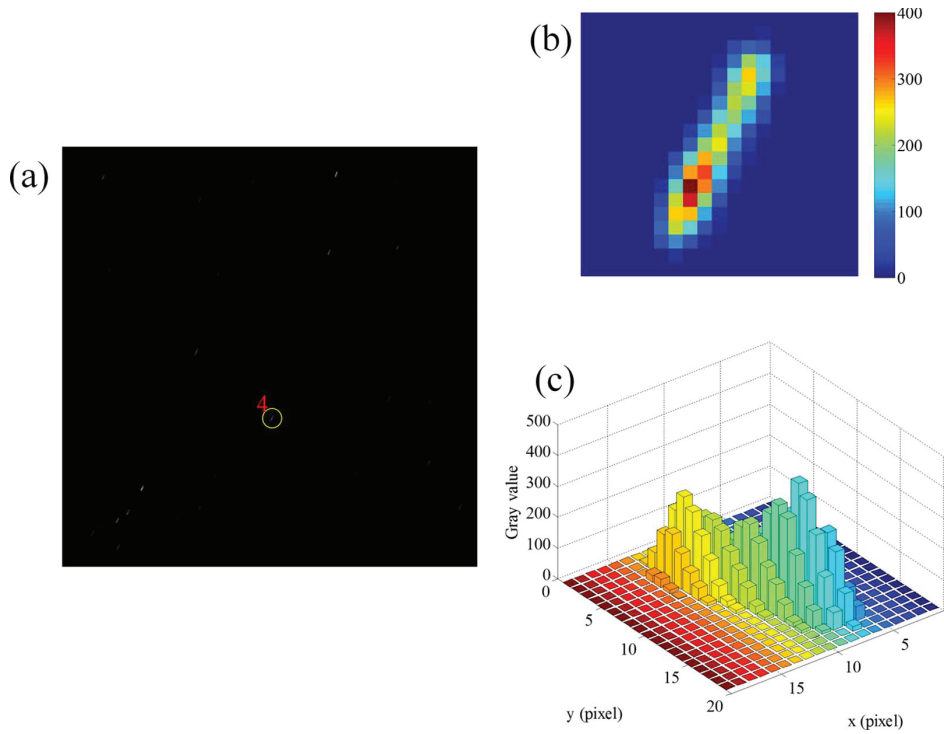
**Fig. 8.** Region extraction result of the identified star (No. 4) after the removal of the background noise. (a) Identified star in the image frame; the grayscale is properly chosen in order to better show the star image in a visual sense. (b) and (c) are the detailed views in color scale and 3D bar plot of the identified star spot of No. 4, respectively.
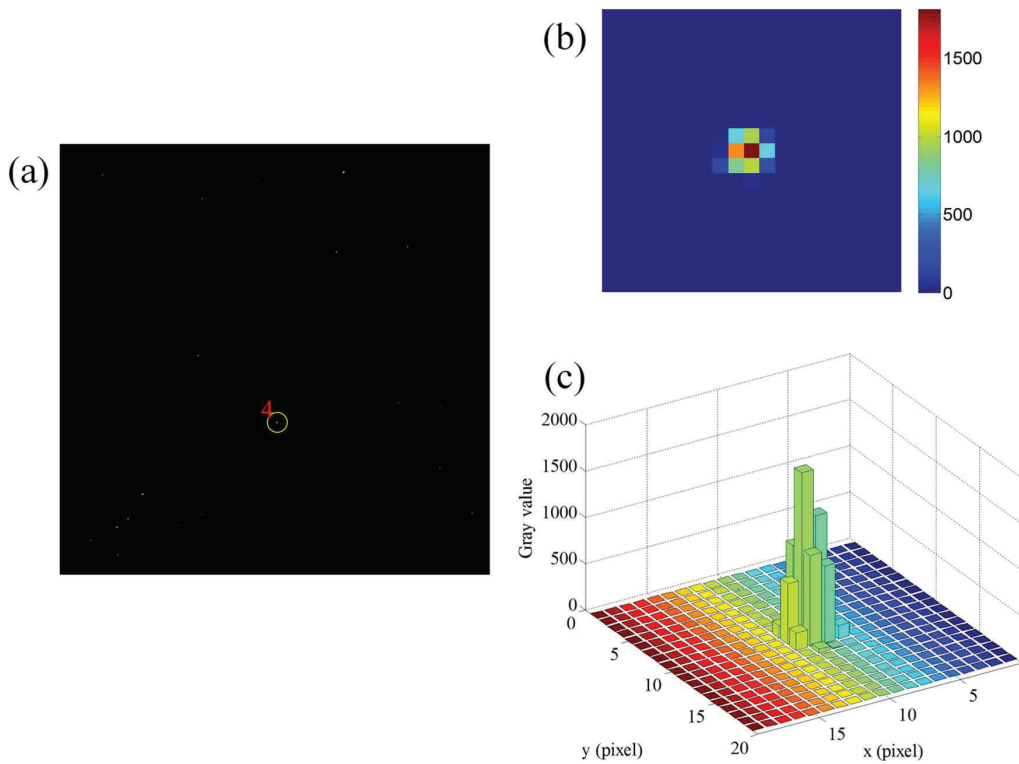


**Fig. 9.** Restored star image (No. 4). (a) Restored star spot in the image frame; the grayscale is properly chosen in order to better show the star image in a visual sense. (b) and (c) are the detailed views in color scale and 3D bar plot of the star spot, respectively.

results obtained without our method are also given: only six brighter stars with higher SNR are identified. Obviously, the region-confined method can work under a much worse conditioned circumstance.

Detailed processing results of the blurred star image with the proposed method are given in Figs. 8 and 9, and the identified star number 4 in Table 3 is chosen as an example. Figure 8 is the star region extraction result after removing the noise. For clarity, the extracted star image is presented in a color map, as shown in Figs. 8(b) and 8(c). With the proposed multi-seed growing method, the motion-blurred star region is successfully extracted and the noise around the regions is cleared thoroughly. It is noted that since further restoration processes will amplify the noise, it is necessary to remove the noise as best as we can previously.

All the extracted star areas are tailored in small blocks from the image frame, and the restoration operation needs to be implemented in these blocks only, which will accelerate the restoration process. Figure 9 gives the detailed restoration result of a motion-blurred star image. From Figs. 9(b) and 9(c), we can see that the restored star image is similar to that under the static conditions. The energy distribution of the star image, which disperses in more than 30 pixels in Fig. 8, is concentrated into about $3 \times 3$ pixels in the restored star spot. The average gray value of the star image increases from about 184 to 864 per pixel. Therefore, the SNR is enhanced by 5–6 times, which is vital for the improvement of the centroiding accuracy and the identification rate.

According to the processing results of the motion-blurred star image above, we can see that the blurred star image region is successfully extracted and restored with our method. The star identification results indicate that our method is much more effective for motion-blurred star images under dynamic conditions.

## 5. CONCLUSIONS

A region-confined restoration method for the motion-blurred star image of the star sensor under dynamic conditions is proposed in this paper. In order to verify the proposed method, simulations and experiments with the star sensor under different dynamic conditions were carried out. Both the simulation and the experimental results show that the region-confined restoration method is effective in the motion-blurred star image processing, and it is adaptive to different dynamic conditions. The noises around the extracted star regions are removed completely with the multi-seed-region growing approach, which is vital for the restoration and the improvement of centroiding accuracy. Time consumption and SNR improvement are both taken into account in the restoration strategy. The identification rate and the average number of the identified star are much better compared to the common methods, which is significant for the further improvement of the attitude determination of a star sensor.

## REFERENCES

1. C. C. Liebe, "Star trackers for attitude determination," IEEE Trans. Aerosp. Electron. Syst. **10**, 10–16 (1995).
2. C. C. Liebe, "Accuracy performance of star tracker-a tutorial," IEEE Trans. Aerosp. Electron. Syst. **38**, 587–599 (2002).
3. C. Liu, G. Liu, X. Wang, and A. Li, *Principles and Systematic Applications of Missile-Borne Star Sensor* (National Defense Industry, 2010).
4. X. Wei, W. Tan, J. Li, and G. Zhang, "Exposure time optimization for highly dynamic star trackers," Sensors **14**, 4914–4931 (2014).
5. J. Shen, G. Zhang, and X. Wei, "Simulation analysis of dynamic working performance for star trackers," J. Opt. Soc. Am. A **27**, 2638–2647 (2010).
6. R. W. H. van Bezooijen, "SIRTF autonomous star tracker," Proc. SPIE **4850**, 108–121 (2003).
7. L. Ma, X. Wang, D. Zhan, and D. Dai, "Extraction method of the motion blurred star image for the star sensor under high dynamic conditions," in *12th IEEE International Conference on Signal Processing*, Hangzhou, 2014.
8. A. Richard, R. Li, and A. Wu, "Method for compensation star motion induced error in a stellar inertial attitude determination system," U.S. patent US7487016B2 (3 February 2009).
9. F. Xing, N. Chen, Z. You, and T. Sun, "A novel approach based on MEMS-Gyro's data coupling for determining the centroid of star spot," Math. Probl. Eng. **2012**, 1–20 (2012).
10. T. Sun, F. Xing, Z. You, and M. Wei, "Motion-blurred star acquisition method of the star tracker under high dynamic conditions," Opt. Express **21**, 20096–20110 (2013).
11. W. Zhang, W. Quan, and L. Guo, "Blurred star image processing for star sensors under dynamic conditions," Sensors **12**, 6712–6726 (2012).
12. T. Sun, F. Xing, Z. You, X. Wang, and B. Lei, "Smearing model and restoration of star image under conditions of variable angular velocity and long exposure time," Opt. Express **22**, 6009–60024 (2014).
13. L. Ma, D. Zhan, G. Jiang, S. Fu, H. Jia, X. Wang, Z. Huang, J. Zheng, F. Hu, W. Wu, and S. Qin, "Attitude-correlated frames approach for a star sensor to improve attitude accuracy under highly dynamic conditions," Appl. Opt. **54**, 7559–7566 (2015).
14. P. G. Savage, *Strapdown Analytics* (Strapdown Associates, 2000).
15. X. Wu and X. Wang, "Multiple blur of star image and the restoration under dynamic conditions," Acta Astronaut. **68**, 1903–1913 (2011).
16. S. Qin, D. Zhan, J. Zheng, W. Wu, H. Jia, S. Fu, and L. Ma, "A dynamic attitude measurement method of star sensor based on gyro's precise angular correlation," U.S. patent 14/569209 (12 December 2014).
17. C. C. Liebe, K. Gromov, and D. M. Meller, "Toward a stellar gyroscope for spacecraft attitude determination," J. Guid. Control Dyn. **27**, 91–99 (2004).
18. R. C. Gonzalez and R. E. Woods, *Digital Image Processing*, 3rd ed. (Pearson Education, 2010), Chap. 9.
19. W. H. Richardson, "Bayesian-based iterative method of image restoration," J. Opt. Soc. Am. A **62**, 55–59 (1972).
20. L. B. Lucy, "An iterative technique for the rectification of observed distribution," Astron. J. **79**, 745–754 (1974).
21. C. Liu, L. Hu, G. Liu, B. Yang, and A. Li, "Kinematic model for the space-variant image motion of star sensors under dynamical conditions," Opt. Eng. **54**, 063104 (2015).
22. C. Padgett and K. K. Delgado, "A grid algorithm for autonomous star identification," IEEE Trans. Aerosp. Electron. Syst. **33**, 202–213 (1997).